A comprehensive study on the characterization of lyzed blood samples using dual-wavelength photoacoustics

Subhadip Paul[1], Hari Shankar Patel[2], Vatsala Misra[3], Ravi Rani[3], Amaresh K. Sahoo[1], Ratan K. Saha*,[1]

[1] Department of Applied Sciences, Indian Institute of Information Technology Allahabad, Jhalwa, Prayagraj, 211015, U.P, India.
[2] Laser Biomedical Applications Division, Raja Ramanna Centre for Advanced Technology, Indore, 452013, M.P., India.
[3] Department of Pathology, Moti Lal Nehru Medical College, Prayagraj, 211002, U.P., India.

* ratank.saha@iiita.ac.in

Abstract

Anemia is a global health concern, prompting the need for rapid and accurate diagnostic tools, especially for vulnerable populations. Estimating the blood lysis level (LL) and oxygen saturation (SO_2) are essential not only for anemia but also for other hemolytic conditions. This study explores the potential of photoacoustic (PA) spectroscopy as a quantitative tool for evaluating hemolysis in anemia diagnosis. In vitro PA measurements on human blood samples were validated through computational modeling using the discrete dipole approximation, Monte Carlo, and k-Wave acoustic simulations. The quantitative values of blood hematocrit (H), LL and SO_2 have been estimated using simulated and experimental PA signals. The wavelength pairs 700-905 nm and 700-1000 nm have been found to be optimal for the simultaneous estimation of these parameters and provided H and SO_2 estimations with accuracy approximately $> 90\%$ up to LL=14% and for LL = 0-30%, respectively. The correlation coefficient between the actual and evaluated lysis levels has been computed to be ≈ 0.90. Further investigation is needed to enhance the robustness and clinical applicability of the developed method under an in vivo setting when both the H and LL levels are not known.

Keywords

Photoacoustics (PAs), Oxygen saturation level (SO_2), Hematocrit level (H), Lysis level (LL), Monte-Carlo simulation (MC), Discrete Dipole Approximation (DDA).

1 Introduction

Hemolysis is the premature destruction of red blood cells (RBCs). It occurs because of the rupture of RBC membranes and causes release of hemoglobin into the bloodstream. It is often linked with underlying health conditions [33]. Excessive hemolysis can contribute to anemia, oxidative damage, jaundice, and renal complications, posing significant health risks [4, 10, 26, 28]. Anemia has always been a global issue, primarily because of iron deficiency. WHO defines anemia as the hemoglobin concentration falling below 12 g/dl and 13 g/dl for females and males, respectively [1]. In a recent study by WHO,

approximately 40% of all children aged 6–59 months, 37% of pregnant women, and 30% of women 15–49 years of age are affected by anemia all over the globe. In southeastern countries, particularly in the Indian subcontinent, anemia cases remain exceptionally high; more than 35% have been recorded [43]. Various factors, including autoimmune disorders, infections, genetic abnormalities, toxins, and mechanical stress, can trigger this process [29, 41, 58, 64]. Early identification of hemolysis is crucial to mitigating complications, yet conventional diagnostic techniques rely on time-intensive laboratory analyses [51]. Methods like visual inspection, Spectrometry (the most accurate one), complete blood counts (CBC) and the heptoglobin test are commonly used for the detection and quantification RBC lysis. Some complicated techniques such as Lactate Dehydrogenase, Genetic test can also be performed for the same purpose [55].

In recent times, the photoacoustic (PA) technique has been evolving as a promising blood characterization tool. The most important feature of this technique is that, in vivo assessment of blood parameters may be possible. Saha et al. compared the PA signal properties of normal and lyzed blood samples at 532 and 1064 nm optical wavelengths [45], [46]. Banerjee et al. studied the dynamical variation of the PA signal profile when RBCs are undergoing lysis using a low-cost 905 nm based PA device [3]. Bodera et al. examined blood clot and blood lysis in vitro using a high-frequency ultrasound detector-based imaging system [7]. Besides these, researchers all over the globe are increasingly using the PA technique for probing blood samples. For example, Yadem et al. have introduced Cytophone, a PA-based flow cytometer to detect malaria infection in the human body [60]. Padmanabhan et al. have developed a PA polarization–enhanced optical rotation sensing system and found chiral molecular concentration for depths up to a few millimeters [34]. A vast amount of work has also been conducted on normal and pathological blood samples by many groups across the globe [9], [17], [39], [38], [25], [48], [47], [44], [23], [37], [36]. [6], [35].

PA emission from blood essentially depends upon its optical properties, namely, absorption coefficient (μ_{abs}), scattering coefficient (μ_{sca}) and anisotropy factor (g). Though these are bulk properties but they are governed by the microscopic features such as spatial organization of RBCs, morphological, biophysical and biochemical properties of individual cells [48], [47], [44], [37], [36]. There exist a number of theoretical methods and numerical schemes which can be used to obtain the optical absorption cross-section, scattering cross-section and g factor of a scatterer [32]. For instance, the Mie theory is applicable for regular shapes [59]. The Born approximation [22] and Wentzel-Kramers-Brillouin approximation work well for weak scattering or slowly varying media [20]. Other common approaches include the T-matrix method [56], the finite element method [30], the finite difference time domain method [16], the ray tracing method [54], the Monte-Carlo method [57], etc. One popular formulation is the discrete dipole approximation (DDA) [12][11][32]. It models a scatterer having an arbitrary shape as a collection of discrete electric dipoles. The knowledge of the refractive indices of both the cell and the surrounding medium are required for its implementation. It can be used to evaluate the optical parameters of RBC as well.

Theoretical studies modeling PA emission from blood consider RBCs as spherical absorbers and thus neglect the actual shape of RBCs [27][18][48]. In this study, we have addressed this gap by incorporating the exact RBC morphology for numerical calculations

of optical absorption cross-section, scattering cross-section and g factor for a healthy RBC exploiting the DDA technique. Freely available discrete dipole scattering (DDSCAT) software implements the DDA formulation. Subsequently, obtained the optical properties (μ_{abs}, μ_{sca} and g) of a blood sample at certain optical wavelengths. A series of lyzed blood samples with initial hematocrit, H=50% and oxygenation, SO_2=68% have been considered. The lysis level has been varied from LL=0 to 30%. The suspending medium has been prepared by mixing hemoglobin molecules in phosphate-buffered saline (PBS) medium or in plasma (PLS) medium. DDSCAT, Monte Carlo and k-Wave simulations have been conducted sequentially to generate the PA signals [36]. Analogous experimental studies (in vitro) have also been carried out with human blood samples. Accordingly, H, LL and SO_2 levels have been estimated from simulated/measured signals using dual wavelength PAs (700-905 and 700-1000 nm wavelength pairs). Simulation and experimental results reveal that accurate estimations of H and LL are possible with accuracy $> 90\%$ up to LL=14% and for SO_2 up to LL=30%. The primary contributions of this work are: i) Determination of the optical parameters (μ_{abs}, μ_{sca} and g) of lyzed blood samples at some specific optical wavelengths and using the DDA model incorporating the biconcave shape of RBCs. ii) Generation of PA signals utilizing the k-Wave toolbox based on the fluence maps provided by the Monte Carlo simulation. iii) Measurement of PA signals from analogous human blood samples. iv) Quantification of the levels of H, LL and SO_2 from simulated and experimental PA signals.

2 Governing theoretical models

2.1 PA wave equation

In practice, short laser pulses illuminate a tissue sample. Photons are absorbed by the sample, causing its rapid thermo-elastic expansion, followed by emission of PA signals. The time-dependent PA wave equation in a 3D generalized coordinate system can be cast as,

$$\left(\nabla^2 - \frac{1}{v^2}\frac{\partial^2}{\partial t^2}\right) p(\mathbf{r}, t) = -\frac{\beta}{\mathrm{C}_P}\frac{\partial \mathscr{H}(\mathbf{r}, t)}{\partial t}. \tag{1}$$

In equation (1), the notations v, β and C_P are the speed of sound in the medium, isobaric volume expansion coefficient, and isobaric specific heat of the source region, respectively; $\mathscr{H}(\mathbf{r}, t)$ the heating function, i.e., the amount of heat deposited per unit time per unit volume and $p(\mathbf{r}, t)$ is the pressure at any arbitrary point at a location $\mathbf{r}$ at time t. The initial pressure rise in the sample due to pulsed laser heating is $p_0 = \mu_{\text{abs}}\Gamma F$ with Γ and F being the Grüneisen parameter and fluence of the laser beam, respectively. The temporal profile of a PA signal depends upon the photon weight deposition map in the tissue.

Photon propagation in a tissue can be modeled using the famous radiative transfer equation (RTE). The RTE is valid for both ballistic and diffusion regimes ($< 100\ \mu m$) [49, 61]. An approximate version of the RTE known as the diffusion equation (DE) can also model the same faithfully when $\mu_{\text{abs}} << \mu_{\text{sca}}$. The DE is given by,

$$\left[\hat{\zeta}.\nabla + (\mu_{\text{sca}} + \mu_{\text{abs}})\right] \mathscr{R}(\mathbf{r}, \hat{\zeta}) \quad = \quad \mu_{\text{sca}} \left(\int_{4\pi} \mathscr{R}(\mathbf{r}, \hat{\zeta}) f(\hat{\zeta}.\hat{\zeta}') d\Omega' \right) \quad + \quad \Sigma(\mathbf{r}, \hat{\zeta}), \quad (2)$$

where, $\mathscr{R}(\mathbf{r}, \hat{\zeta})$ is the time-independent radiance; ζ and ζ' are the direction vectors of scattered and incident light; $\Sigma(\mathbf{r}, \hat{\zeta})$ is the source term. If it is assumed that, $\mathscr{H}(\mathbf{r}, t) = I_0(\mathbf{r})\mu_{\text{abs}} e^{-i\omega t}$, then one can write,

$$I_0(\mathbf{r}, t) = \int_{4\pi} \tilde{\mathscr{R}}(\mathbf{r}, \hat{\zeta}, t) d\Omega, \quad (3)$$

and

$$F(\mathbf{r}) = \int_{-\infty}^{\infty} I_0(\mathbf{r}, t) dt, \quad (4)$$

here, $d\Omega$ indicates the solid angle through which scattered photons pass. Note that $\tilde{\mathscr{R}}(\mathbf{r}, \hat{\zeta}, t)$ is the time-dependent radiance; $\tilde{\mathscr{R}}(\mathbf{r}, \hat{\zeta}, t)$ and $\mathscr{R}(\mathbf{r}, \hat{\zeta})$ are the Fourier transform pairs. Equation (2) is not analytically solvable. Thus, the Monte Carlo simulation technique is generally applied. The optical properties of the tissue ($\mu_{\text{abs}}, \mu_{\text{sca}}$ and g) have to be known for this purpose and thus, these quantities are defined in the next sections.

2.2 The discrete dipole approximation

The complete derivation of the mathematical model of the DDA can be found else where Draine et al. [12, 14, 15]. However, the background theory has been summarized below for the sake of completeness of this study. For a fixed target geometry in a coordinate system $\hat{x}, \hat{y}, \hat{z}$, we generate a dipole array. It aims to obtain a self-consistent set of dipole moments $\mathbf{P}_j$, $(j = 1, \ldots, N)$ so that $\mathbf{P}_j = \alpha_j \mathbf{E}_{\text{loc},j}$, where, α_j: polarizability and $\mathbf{E}_{\text{loc},j}$: local electric field at dipole point j. As noted by Purcell and Pennypacker (1973) and Yung (1978), this can be, in terms of complex vectors, written as N simultaneous equations of the form[40], [63]

$$\mathbf{P}_j = \alpha_j \left(\mathbf{E}_{\text{inc},j} - \sum_{m \neq j} \mathbf{A}_{jm} \mathbf{P}_m \right), \quad (5)$$

$\mathbf{E}_{\text{inc},j}$ is the electric field at position j due to the incident plane wave, $\mathbf{E}_{\text{inc},j} = \mathbf{E}_0 \exp(i\mathbf{k} \cdot \mathbf{r}_j - i\omega t)$, and $\mathbf{A}_{jm}\mathbf{P}_m$ is the contribution to the electric field at position j due to the dipole at position m:

$$\mathbf{A}_{jm}\mathbf{P}_m = \frac{\exp(ikr_{jm})}{r_{jm}^3} \left\{ k^2 \mathbf{r}_{jm} \times (\mathbf{r}_{jm} \times \mathbf{P}_m) + \frac{(1 - ikr_{jm})}{r_{jm}^2} \left[\mathbf{r}_{jm}^2 \mathbf{P}_m - 3\mathbf{r}_{jm}(\mathbf{r}_{jm} \cdot \mathbf{P}_m) \right] \right\}, \quad (j \neq m). \quad (6)$$

where $r_{jm} = |\mathbf{r}_j - \mathbf{r}_m|$. Equation (6) serves to define the matrices $\mathbf{A}_{jm}$ for $j \neq m$. It is convenient to define also matrices $\mathbf{A}_{jj} = \alpha_j^{-1}$, so that the scattering problem can be compactly formulated as a set of N inhomogeneous linear complex vector equations:

$$\sum_{m=1}^{N} \mathbf{A}_{jm} \mathbf{P}_m = \mathbf{E}_{\text{inc},j} \quad (j = 1, \ldots, N), \quad (7)$$

here, $(A_{jl})_{mi} = (A_{lj})_{im}$, i.e, the $\mathbf{A}_{jm}$ are 3×3 matrices symmetric.

2.3 Extinction, absorption and scattering efficiency factors

Once the polarisation $\mathbf{P}_j$ is known, the extinction coefficient factor for the grain is computed from the forward-scattering amplitude using the optical theorem,[14, 50]

$$\mathrm{Q_{ext}} = \frac{4k}{\mathtt{a}_{\mathtt{eff}}^2 |\mathbf{E}_{inc}|^2} \sum_{j=1}^{N} \mathrm{Im}(\mathbf{E}^*_{inc,j} \cdot \mathbf{P}_j), \tag{8}$$

$\mathtt{a}_{\mathtt{eff}}$ is the effective radius of a RBC. The absorption coefficient factor is obtained by summing over the energy dissipation rate of each dipole. By substituting $\mathbf{P} = \alpha \mathbf{E}_{inc}$ into Eq. (8), the extinction coefficient factor can readily be obtained from the optical theorem as, [12]

$$\mathrm{Q_{ext}} = \frac{4k}{\mathtt{a}_{\mathtt{eff}}^2 |\mathbf{E}_{\mathrm{inc}}|^2} \sum_{j=1}^{N} \mathrm{Im}(\mathbf{P} \cdot (\alpha^{-1})^* \mathbf{P}^*). \tag{9}$$

Note that for isotropic polarizability it reduces to $\mathrm{Q_{ext}} = 4\pi k \mathrm{Im}(\alpha)$.

Thus, the absorption coefficient factor for the entire grain is [13]

$$\mathrm{Q_{abs}} = \frac{4k}{\mathtt{a}_{\mathtt{eff}}^2 |\mathbf{E}_{\mathrm{inc}}|^2} \sum_{j=1}^{N} \left\{ \mathrm{Im}[\mathbf{P_j} \cdot (\alpha_j^{-1})^* \mathbf{P_j}^*] - \frac{2k^3}{3} \mathbf{P_j} \cdot \mathbf{P_j}^* \right\}. \tag{10}$$

The scattering coefficient factor can, in principle, be obtained from the difference between the extinction and absorption coefficient factors: [13]

$$\mathrm{Q_{sca}} = \frac{k^4}{\pi \mathtt{a}_{\mathtt{eff}}^2 |\mathbf{E}_{\mathrm{inc}}|^2} \int d\Omega \left| \sum_{j=1}^{N} [\mathbf{P}_j - \hat{n}(\hat{n} \cdot \mathbf{P}_j)] \exp(-ik\hat{n} \cdot \mathbf{r}_j) \right|^2, \tag{11}$$

where $\hat{n}$ is a unit vector in the direction of scattering. It is also of interest to evaluate the scattering asymmetry parameter, $g \equiv \langle \cos\theta \rangle$, which is given by, [12]

$$g = \frac{k^3}{\pi \mathtt{a}_{\mathtt{eff}}^2 \mathrm{Q_{sca}} |\mathbf{E}_{\mathrm{inc}}|^2} \int d\Omega \, (\hat{n} \cdot \mathbf{k}) \left| \sum_{j=1}^{N} [\mathbf{P}_j - \hat{n}(\hat{n} \cdot \mathbf{P}_j)] \exp(-ik\hat{n} \cdot \mathbf{r}_j) \right|^2.$$

It varies from -1 to 1.

3 Materials and methods

3.1 Numerical investigation

3.1.1 Calculation of optical absorption coefficient and complex refractive index

A healthy RBC typically occupies a volume of $V_{\mathrm{RBC}} = 91.52$ fL and retains 281 million hemoglobin molecules having a molar mass of 64500 g; 66% of V_{RBC} is water [36, 52].

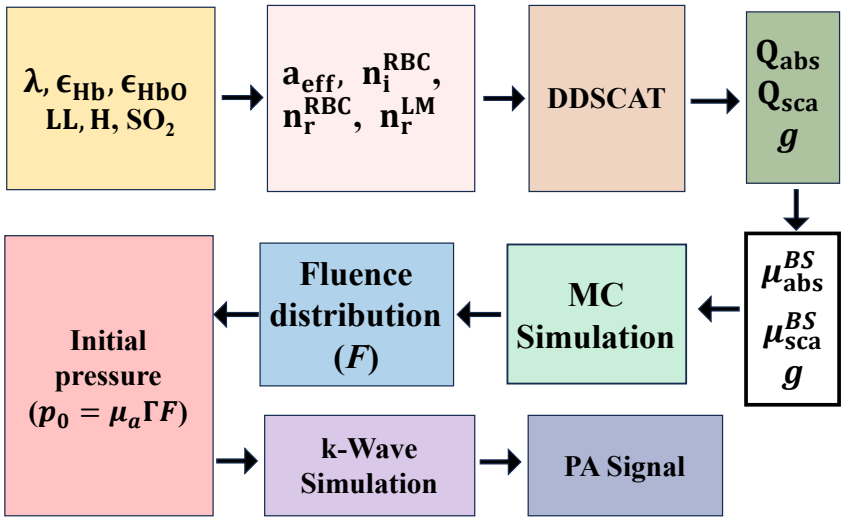

Figure 1. Workflow diagram illustrating the simulation pipeline implemented for modeling various lysis levels of RBC samples in PBS and PLS suspending media.

Based on these, the optical absorption coefficient for the semi-solid medium present inside RBC could be expressed as,

$$\mu_{\text{abs}}^{\text{RBC}} = 2.303\,(\text{C}_{\text{HbO}}\varepsilon_{\text{HbO}} + \text{C}_{\text{Hb}}\varepsilon_{\text{Hb}}) + 0.66\mu_{\text{abs}}^{\text{W}}, \tag{12}$$

Table 1. Tabulated values of the real (n_r^{LM}) and imaginary (n_i^{LM}) components of the refractive index for the suspending lyzed media (PBS/PLS based) across different stages of lysis.

λ (nm)	Blood sample		PBS				PLS			
	H (%)	LL (%)	$\mu_{\text{abs}}^{\text{LM}}$ (cm^{-1})	$\text{n}_\text{r}^{\text{LM}}$	$\text{n}_\text{i}^{\text{LM}}$ ($\times 10^{-5}$)	$\mu_{\text{abs}}^{\text{BS}}$ (cm^{-1})	$\mu_{\text{abs}}^{\text{LM}}$ (cm^{-1})	$\text{n}_\text{r}^{\text{LM}}$	$\text{n}_\text{i}^{\text{LM}}$ ($\times 10^{-5}$)	$\mu_{\text{abs}}^{\text{BS}}$ (cm^{-1})
700	50	0	0.021	1.331	0.010	4.545	0.042	1.344	0.020	4.556
	47	6	0.533	1.336	0.300	4.545	0.553	1.349	0.310	4.556
	43	14	1.132	1.342	0.630	4.545	1.151	1.354	0.640	4.556
	40	20	1.529	1.346	0.850	4.545	1.547	1.358	0.860	4.556
	35	30	2.109	1.351	1.170	4.545	2.125	1.364	1.180	4.556
905	50	0	0.053	1.328	0.040	6.307	0.126	1.338	0.090	6.344
	47	6	0.761	1.333	0.550	6.307	0.830	1.343	0.600	6.344
	43	14	1.589	1.339	1.140	6.307	1.654	1.349	1.190	6.344
	40	20	2.138	1.343	1.540	6.307	2.199	1.353	1.580	6.344
	35	30	2.940	1.348	2.120	6.307	2.996	1.358	2.160	6.344
1000	50	0	0.464	1.327	0.370	4.861	0.305	1.337	0.240	4.781
	47	6	0.962	1.332	0.770	4.861	0.812	1.342	0.650	4.781
	43	14	1.544	1.338	1.230	4.861	1.405	1.348	1.120	4.781
	40	20	1.930	1.342	1.540	4.861	1.797	1.352	1.430	4.781
	35	30	2.494	1.348	1.980	4.861	2.371	1.358	1.890	4.781

where C_{HbO} and ε_{HbO} are the molar concentration and extinction coefficient for oxy-hemoglobin (HbO), respectively; the same quantities for deoxy-hemoglobin (Hb) are denoted by C_{Hb} and ε_{Hb}, respectively; μ_{abs}^{W} is the optical absorption coefficient for water (`https://www.omlc.in`) . Accordingly, real and imaginary parts of the refractive index for the same cellular matrix could be estimated to be [19],

$$\mathtt{n}_{\mathtt{r}}^{RBC} = \mathtt{n}_{\mathtt{r}}^{M}[\mathscr{B}(C_{HbO} + C_{Hb}) + 1], \tag{13}$$

$$\mathtt{n}_{\mathtt{i}}^{RBC} = \frac{\mu_{abs}^{RBC}\lambda}{4\pi}, \tag{14}$$

respectively. Here, $\mathscr{B}$: wavelength-dependent specific refractive index increment [31]. The numerical values of these quantities for a RBC with oxygen saturation $SO_2 = 0.68$ could be computed to be, $\mu_{abs}^{rbc} = 9.070, 12.563$ and 9.258 cm^{-1}, $\mathtt{n}_{\mathtt{r}}^{rbc} = 1.418, 1.415$ and 1.417 and $\mathtt{n}_{\mathtt{i}}^{rbc} = 5.050 \times 10^{-5}, 9.050 \times 10^{-5}$ and 7.370×10^{-5} at 700, 905 and 1000 nm, respectively, assuming $C_{HbO} + C_{Hb} = 5.1 \times 10^{-3}$ mole/L.

The optical absorption coefficient for the extracellular matrix significantly changes in the presence of freely suspending hemoglobin molecules, occurring because of the lysis of RBCs. It could be estimated by evaluating the following formula,

$$\mu_{abs}^{LM} = \frac{1}{(1 - H + H\ LL)}\Big[H\ LL\mu_{abs}^{RBC} + (1 - H)\mu_{abs}^{M}\Big], \tag{15}$$

where, LL is the lysis level and H is the hematocrit (at LL = 0%) of the sample; the subscript LM indicates PBS or PLS based lyzed medium. Table 1 displays the computed values of μ_{abs}^{LM} and refractive index for a series of blood samples having different lysis levels but with $H = 0.50$ and $SO_2 = 0.68$. The same quantity for the whole blood (μ_{abs}^{BS}) could also be determined as (by adding the contributions from intact RBCs and surrounding medium),

$$\mu_{abs}^{BS} = H\big(1 - LL\big)\mu_{abs}^{RBC} + \big(1 - H + H\ LL\big)\mu_{abs}^{LM}, \tag{16}$$

subscript BS states blood sample; its numerical values are included in the same table (columns 6 and 10 for PBS and PLS media, respectively of Table 1).

3.1.2 DDA simulation

The RBC model was designed in Blender 4.2, an open-source software. Normal RBC looks like a biconcave disk [5, 27, 52]. Figure 2 shows the meridional cross-section of a biconcave RBC, defined by four critical morphological parameters: the diameter (D), the dimple thickness (t), the maximum thickness (h), and the diameter (d) of the circle determining the location of the maximum thickness. The chosen values of that morphological parameter were $D = 8.40$ μm, $t = 0.85$ μm, $h = 2.04$ μm, and $d = 5.88$ μm providing an effective radius, $\mathtt{a}_{\mathtt{eff}} = 2.79$ μm.

The DDSCAT module is an open-source Fortran-based algorithm [13]. The DDSCAT version 7.3.1 was employed, and single precision mode was used to execute the DDA simulations. The DDSCAT simulation was configured by selecting specific options for key parameters. Radiative torque calculations were disabled. The conjugate gradient

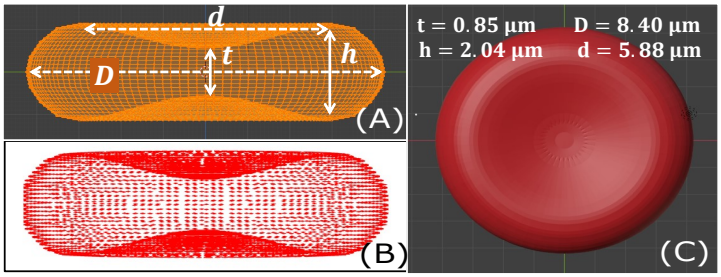

Figure 2. Visualization of red blood cell (RBC) geometry. (A) Side view of the RBC structure. (B) Dipole distribution used for electromagnetic modeling. (C) Top view highlighting the characteristic biconcave shape.

solver was chosen as preconditioned Bi-Conjugate Gradient Stabilized. The Fast Fourier Transforms were performed using the Generalized Prime Factor Algorithm method. The dipole polarizability was computed using the Generalized Kernel Dipole Layered Dipole Regularization technique. Finally, binary output files were avoided during the simulation. The computational volume in DDSCAT was set to $230 \times 230 \times 80$ voxels containing cubic lattice points. The RBC model was discretized into approximately 1.6×10^6 dipoles for the wavelengths of interest (i.e., 700, 905, 1000 nm) using the DDSCAT-convert module available on `nanoHUB.org` [see Fig. 2(B)]. The refractive indices ($\mathtt{n_r}$ and $\mathtt{n_i}$) of the RBC and the surrounding medium were determined and presented in Table 1). The error tolerance and maximum number of iterations were set to 10^{-5} and 1000, respectively. A total of 125 orientation-average was considered to yield $\mathrm{Q_{abs}}$, $\mathrm{Q_{sca}}$ and g. All computations were performed on a high-performance workstation equipped with 256 GB RAM, an AMD Ryzen Threadripper PRO 5965WX 24-core processor (3.80 GHz), 932 GB SSD, and 7.28 TB HDD storage. Depending on the chosen H and LL levels, $\mu_{\mathrm{abs}}^{\mathrm{BS}}$ and $\mu_{\mathrm{sca}}^{\mathrm{BS}}$ were calculated using the formulae given below [8], [37], [36]

$$\mu_{\mathtt{abs}}^{\mathtt{BS}} = \frac{\mathrm{H}}{V_{\mathrm{RBC}}} \mathrm{Q_{abs}} \pi \mathtt{a}_{\mathtt{eff}}^2, \tag{17}$$

$$\mu_{\mathtt{sca}}^{\mathtt{BS}} = \frac{\mathrm{H}}{V_{\mathrm{RBC}}} (1-\mathrm{H})^2 \mathrm{Q_{sca}} \pi \mathtt{a}_{\mathtt{eff}}^2, \tag{18}$$

numerical value of g was provided by the DDSCAT as well.

3.1.3 Monte-Carlo and k-Wave simulations

The Monte Carlo Multilayered (MCML) algorithm was utilized to model photon transport in homogeneous blood samples vis-à-vis to obtain the fluence matrix (F) [57]. The simulation domain consisted of a cubic tissue volume with dimensions $200 \times 200 \times 200$ voxels, where each voxel was fixed to be $dx \times dy \times dz = 0.005 \times 0.005 \times 0.005$ cm^3. The optical properties ($\mu_{\mathrm{abs}}^{\mathrm{BS}}$, $\mu_{\mathrm{sca}}^{\mathrm{BS}}$, and g) at a particular wavelength of each voxel were assigned according to Table 2, corresponding to the distinct blood sample under investigation. We introduced $\pm 1\%$ random fluctuations in $\mu_{\mathrm{abs}}^{\mathrm{BS}}$ for 10% of randomly selected voxels to introduce a little randomness, simulating a real condition. The incident laser beam had a diameter of $D_B = 0.10$ cm and featured a uniform lateral spatial profile along with a delta-function temporal profile. For each simulation, 2×10^6 photons were launched

Table 2. DDSCAT based computation of absorption, scattering, and anisotropy coefficients across different lysis levels in an ambient environment (initial surrounding medium was PBS or PLS).

H =50%, SO_2 = 68%		DDSCAT (PBS)					DDSCAT (PLS)				
λ (nm)	LL (%)	$Q_{abs} \times 10^{-5}$	μ_{abs}^{BS} (cm^{-1})	Q_{sca}	μ_{sca}^{BS} (cm^{-1})	g	$Q_{abs} \times 10^{-5}$	μ_{abs}^{BS} (cm^{-1})	Q_{sca}	μ_{sca}^{BS} (cm^{-1})	g
700	0	389.4	5.203	3.045	1017.2	0.991	385.0	5.144	2.738	914.5	0.992
	6	387.8	4.870	2.927	1032.8	0.991	383.0	4.810	2.604	918.6	0.993
	14	385.7	4.432	2.785	1040.9	0.992	380.4	4.371	2.424	905.1	0.993
	20	384.2	4.107	2.689	1034.9	0.992	378.6	4.047	2.287	880.2	0.994
	30	381.9	3.572	2.530	999.8	0.993	375.7	3.514	2.065	816.3	0.994
905	0	539.9	7.214	2.571	858.9	0.989	534.6	7.143	2.317	773.9	0.990
	6	537.4	6.750	2.453	865.6	0.990	531.7	6.678	2.166	764.3	0.991
	14	534.2	6.138	2.297	857.5	0.990	528.1	6.068	1.969	735.3	0.991
	20	532.0	5.687	2.182	839.8	0.990	525.5	5.617	1.830	704.2	0.991
	30	528.5	4.943	1.994	788.1	0.991	521.2	4.875	1.609	635.8	0.992
1000	0	399.4	5.337	2.461	822.0	0.988	395.5	5.285	2.206	737.0	0.989
	6	397.5	4.992	2.335	823.9	0.988	393.3	4.940	2.050	723.3	0.989
	14	395.0	4.539	2.170	810.0	0.989	390.5	4.487	1.850	690.5	0.990
	20	393.3	4.204	2.051	789.4	0.989	388.6	4.154	1.711	658.6	0.990
	30	390.6	3.654	1.859	734.6	0.990	385.5	3.606	1.498	591.9	0.990

with reflections enabled only at the top surface ($z = 0$), while for the side and bottom walls, reflections were disabled. The fluence maps were generated for a specific sample at $\lambda = 700$, 905, and 1000 nm. A schematic of the simulation setup was shown in Fig. 3 of [37]

After calculating the fluence matrix (F), the k-Wave toolbox was used to perform 3D acoustic simulations (Fig.1). The initial pressure rise was computed as $p_0 = \Gamma \mu_{\text{abs}} F$, where $\Gamma = 1$ for all samples. The simulation domain size was $240 \times 240 \times 280$ with a grid spacing of $dx = dy = dz = 0.005$ cm. A perfectly matched layer (PML) of thickness 0.05 cm was employed, with an anisotropic absorption coefficient of 100 np/m to diminish boundary reflections. A spherically focused circular aperture ultrasound transducer (UST) with a radius of 0.05 cm was placed at $(120, 120, 260)$ grid location. Focal point of the transducer was fixed at the center of the computational domain $(120, 120, 100)$. The sensor consisted of 317 grid points, with a center frequency of 5 MHz and a 70% fractional bandwidth. The speed of sound ($v_s = v_M = 1500$ m/s) and density ($\rho_s = \rho_M = 1000$ kg/m^3) remained uniform throughout the computational domain. The Courant–Friedrichs–Lewy number was set to 0.3, achieving numerical stability and providing a time step of 20 ns. A Gaussian noise was added to the simulated pressure signals to achieve 40 dB signal-to-noise ratio.

3.2 Experimental procedure

3.2.1 Sample preparation

Fresh human whole blood samples were obtained from a local blood bank. All five donors were healthy individuals aged between 25 and 40 years. The samples were collected in vacutainer tubes containing EDTA as an anticoagulant agent. A complete report of various blood parameters for each donor is provided in Table 3. This project was cleared apriori by the ethical committee of the institute. For sample preparation, the blood samples were centrifuged at ×1000 g for 15 minutes at room temperature. Blood plasma was carefully extracted and the buffy coat layer was also meticulously discarded. The packed RBCs were then evenly divided into two separate tubes. Plasma was poured into one tube, while phosphate-buffered saline (PBS) was added to the other, ensuring that both samples maintained the same hematocrit level of 50%. This procedure was consistently followed for all donors to prepare a total of 10 samples. In the next step, individual samples were further divided into two parts. One part was subject to complete lysis using an ultrasound sonicator (Qsonica, XL-2000 series, 5W emission, 5-second pulse). The lyzed solution was further centrifuged to discard the debris. The other half was left intact. A series of lyzed samples was prepared by mixing the 100% and 0% lyzed solutions in different ratios, achieving LL = 0%, 6%, 14%, 20%, and 30% lysis

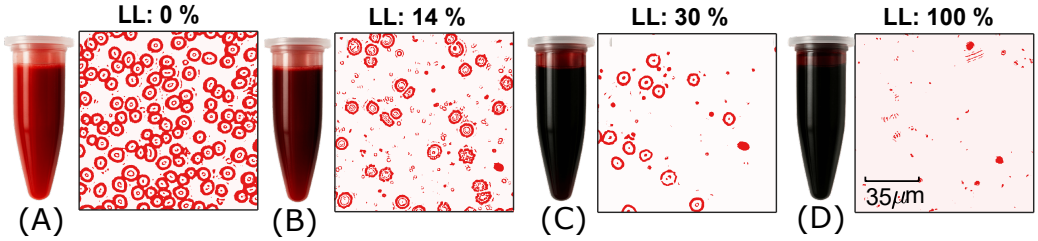

Figure 3. The figure represents (A–D) Blood samples at the lysis levels of LL=0%, 14%, 30%, and 100%, with corresponding microscopic images of smeared samples on glass slides. Scale bar: 35 μm.

Table 3. Summary of demographic details and hematological indices of blood donors, showing inter-individual variability in key parameters including hematocrit (H), total hemoglobin (THB), mean corpuscular volume (MCV), mean corpuscular hemoglobin (MCH), mean corpuscular hemoglobin concentration (MCHC), red cell distribution width (RDW), and red blood cell count (RBC).

Donor	Age (yr)	Gender	H (%)	THB (g/dL)	MCV (fL)	MCH (pg)	MCHC (g/dL)	RDW (%)	RBC ($10^6/\mu L$)
1	28	Male	44.3	14.7	78.7	26.2	33.2	14.7	5.63
2	32	Female	41.8	14.0	81.2	27.2	33.4	13.7	5.13
3	35	Male	49.1	16.4	89.8	29.9	33.3	15.0	5.46
4	40	Male	54.8	16.4	77.7	23.3	30.0	77.5	7.05
5	35	Male	42.6	13.9	99.6	32.4	32.5	86.8	4.28

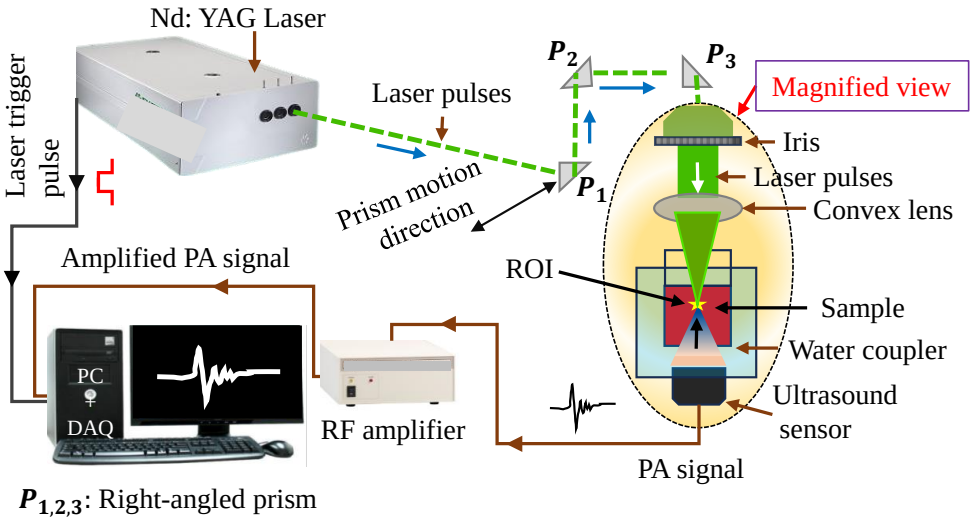

Figure 4. Schematic diagram of the Nd:YAG laser-based PA experimental setup.

levels. A blood sample of approximately 800 µL was placed in a cylindrical sample holder for subsequent PA experiment. Some representative images of lyzed blood samples and the corresponding microscopic images are demonstrated in Fig. 3. The number of cells decreases with increasing lysis.

3.2.2 PA signal detection

The PA experimental setup is shown in Fig. 4. A Nd: YAG laser source (EKSPLA NT352) was employed to perform the measurements. It is a solid-state, Q-switched, tunable and pulsed laser source emitting pulses of 6 ns width at a 10 Hz repetition frequency. This instrument is capable of emitting a range of wavelengths from 335 nm to 2500 nm (excluding the optical range 501-659 nm, but including 532 nm). Three prisms (P_1, P_2, P_3) were used to guide the laser beam. The beam was shaped and focused to a spot using an iris and a convex lens. A spherically focused ultrasound transducer (ISR053) with a center frequency of 5 MHz, bandwidth of 70% and focal length of 25 mm was mounted at the bottom of the sample holder. It was acoustically coupled through water. A data acquisition card (ADLINK PCIe-9852) was used to record the captured PA signals at a sampling frequency of 50 MHz; each signal contained 5000 samples. For each blood sample, a total of 100 RF signals were stored. The PA measurements were conducted at optical wavelengths of 700, 905, and 1000 nm, using optical fluences of 5.5, 19.0, and 47 mJ/cm^2, respectively, to remain within the ANSI safety limits [2]. The exact H level was determined using a micro-capillary centrifuge rotating at 8500 rpm for 2 minutes. UV-Vis spectrophotometric data were also collected for the blood samples with 0% and 30% lysis levels between the wavelength range 500-1100 nm (PerkinElmer Lambda 365+). The blood SO_2 level was assessed utilizing measured UV-Vis data.

3.3 Analysis of PA signals and quantification of Hb concentration and SO_2 levels

The total hemoglobin concentration (THB) and oxygen saturation of a blood sample can be assessed if PA signals are measured at two optical wavelengths by exploiting the following formulae [23, 47],

$$\mathrm{THB} = \frac{P_p(\lambda_1)\Delta\epsilon^{(\lambda_2)} - P_p(\lambda_2)\Delta\epsilon^{(\lambda_1)}}{\epsilon_{Hb}^{(\lambda_1)}\epsilon_{HbO}^{(\lambda_2)} - \epsilon_{Hb}^{(\lambda_2)}\epsilon_{HbO}^{(\lambda_1)}} \tag{19}$$

and

$$\mathrm{SO_2} = \frac{P_p(\lambda_2)\epsilon_{Hb}^{(\lambda_1)} - P_p(\lambda_1)\epsilon_{Hb}^{(\lambda_2)}}{P_p(\lambda_1)\Delta\epsilon_b^{(\lambda_2)} - P_p(\lambda_2)\Delta\epsilon_b^{(\lambda_1)}} \tag{20}$$

respectively and $\Delta\epsilon_b^{(\lambda)} = \epsilon_{\mathrm{HbO}}^{(\lambda)} - \epsilon_{\mathrm{Hb}}^{(\lambda)}$. Here, P_p is the peak-to-peak amplitude of the PA signal. The blood sample with highest hematocrit for each batch was considered as the calibration sample using which the H levels were determined for other samples.

4 Results

4.1 Simulation results

Let us begin with angular scattering patterns for a healthy RBC generated by the DDSCAT module. We considered three orientations of the scattering object as can be visualized from Fig. 5(A)-(C). The direction of the incident light is shown in Fig. 5(A). The scattering planes are chosen perpendicular to each other, i.e., lying on the xy and zx-planes, and the detectors are placed over 0-180^o. Figure 5(a)-(c) plots the corresponding angular distributions of scattering amplitude (S_{11}) for 1000 nm incident light recorded at those scattering planes. It is evident from Fig. 5(a) that the calculated S_{11} for both the detection planes are overlapped since the source look identical for these planes. Similarly, Fig. 5(b) and (c) presents that S_{11} curves are getting separated and switch position because of the symmetry possessed by the biconcave shape. The μ_{abs}, μ_{sca}, and g spectra were calculated using the DDSCAT software are plotted in Fig. 6(A)-(C) for an optical spectral range of 400-1000 nm with H =50%, SO_2 = 68%, LL = 0% and for the PBS suspending medium.

Photon-weight deposition maps generated by the MC simulation are shown in Fig. 7 for blood samples with initial hematocrit level, H=50% and lysis levels LL=0% and 30% for the illuminating wavelengths of 700, 905, and 1000 nm. The nominal oxygenation level is fixed at SO_2 = 68% and PBS is the suspending medium. A color bar tied to the figure quantifies the color code. The optical parameters ($\mu_{\mathrm{abs}}^{\mathrm{BS}}$, $\mu_{\mathrm{sca}}^{\mathrm{BS}}$, and g) are provided in each figure. The photons incident from the top surface, z = 0. It can be seen from this figure that photons are diffused vis-á-vis penetrate less in the blood sample with LL=0% compared to that of LL=30% [compare top and bottom rows of Fig. 7]. This is because $\mu_{\mathrm{abs}}^{\mathrm{BS}}$ is higher at the former sample than the later one and is also true for all incident

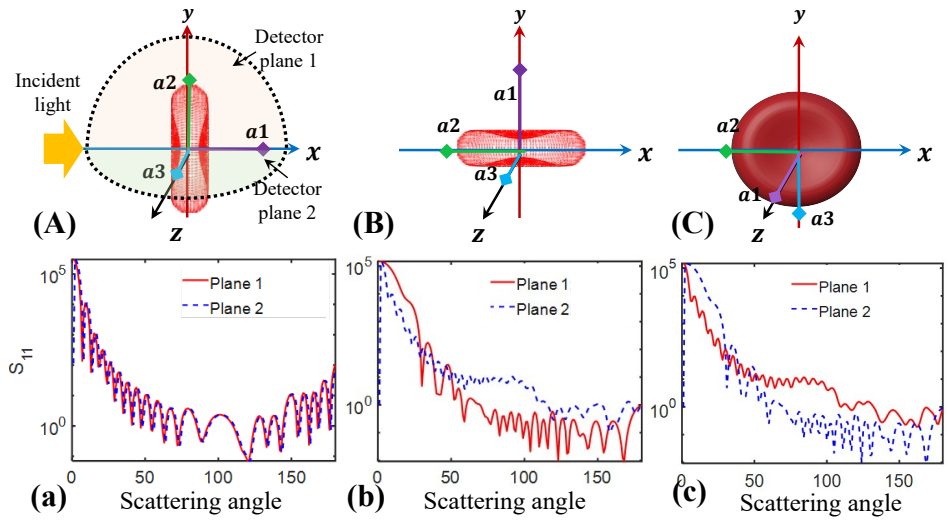

Figure 5. (A)-(C) The schematic diagram showing various orientations of RBC; $a1$, $a2$ and $a3$ are the axes associated with the object frame. The direction of the incident light and detection planes are defined with respect to the laboratory frame, in (A). (a)-(c) The corresponding plots of angular distribution of scattering amplitude (S_{11}) computed at two specific scattering planes for 1000 nm incident optical wavelength.

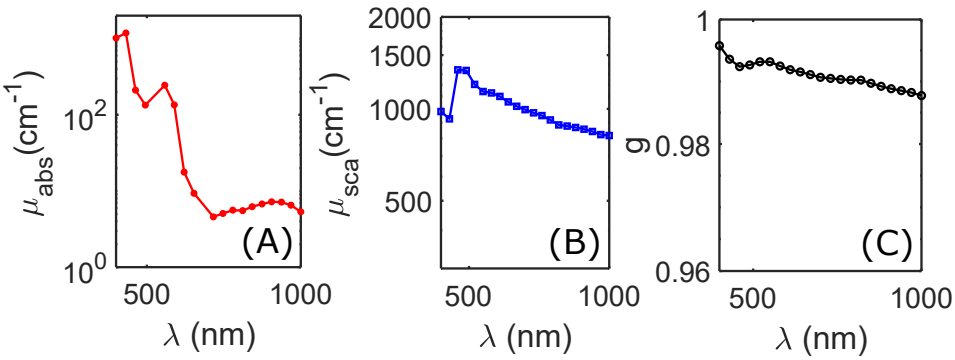

Figure 6. The plots of- (A) absorption coefficient (μ_{abs}), (B) scattering coefficient (μ_{sca}) and (C) anisotropy coefficient (g) spectra for a blood sample with hematocrit H = 50%, SO_2 = 68% and LL = 0%. The results are generated using the DDSCAT module with PBS as the surrounding medium.

optical wavelengths. In both media, P_p values at 905 nm are higher than those at 700 and 1000 nm. Further, the lines for 700 and 1000 nm are nearly overlapping. This observation is consistent with the fluence distribution maps (Fig. 7) and the PA signal profiles [see Fig. 8, panels (A)–(c), left panel]. It is clear that PA amplitude drops by nearly 35% at 700 and 905 nm as the LL increases from 0 to 30% and the same value is about 39% at 1000 nm [see Fig. 9(A)]. The estimated SO_2 values for PBS and PLS media are plotted in panels (G) and (g) of Fig. 9, respectively, alongside the corresponding nominal LL values across the same wavelength combinations. For the 700-905 nm and 700-1000 nm wavelength pairs, the SO_2 estimates remain nearly constant with increasing LL. The corresponding PA signal profiles computed using the k-Wave toolbox for LL = 0% and

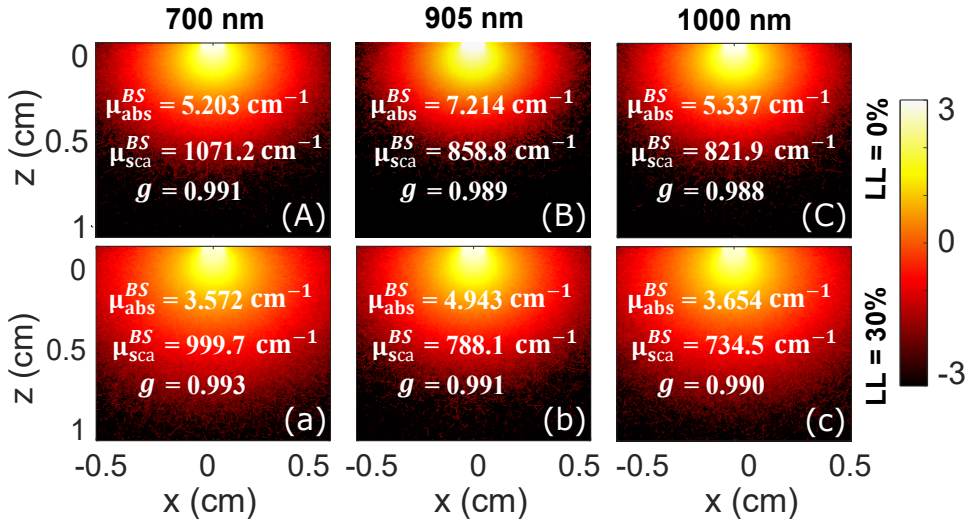

Figure 7. Cross-sectional views of fluence distribution in PBS-based lyzed blood samples at 700, 905 and 1000 nm for LL=0% and 30% lysis levels with SO_2 = 68% and initial hematocrit level, H=50%.

30% are shown in the left panel of Fig. 8 (A)–(C) and (a)–(c), respectively. The PA signal strength at LL=0% is greater than that of LL=30%. Moreover, signal amplitude is consistently stronger at 905 nm than the other wavelengths. This is attributed to the higher values of $\mu_{\text{abs}}^{\text{BS}}$ at 905 nm for both LL=0% and 30% than those of the other wavelengths, as expected. The panels (A) and (a) of Fig. 9 display how P_p varies with lysis level ranging from 0% to 30% for PBS and PLS suspending media, respectively at the optical wavelengths of 700, 905 and 1000 nm. The P_p exhibits an almost linear decrease with increasing LL.

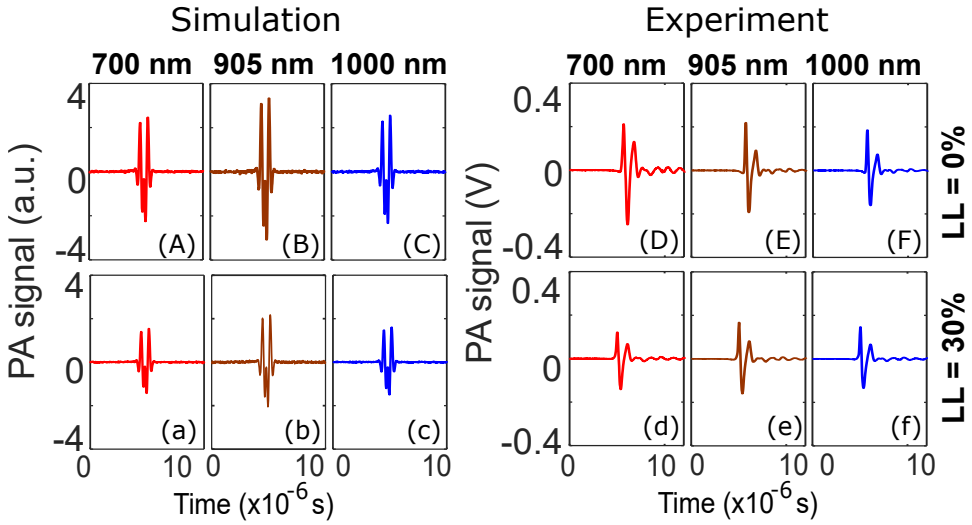

Figure 8. Left panel: Demonstration of the simulated PA signals for LL=0% (A-C, top panel) and LL=30% (a-c, bottom panel) lyzed blood samples at 700, 905, and 1000 nm wavelengths, SO_2 = 68% and initial hematocrit level, H=50%. Right panel: Similar plots for the experimentally measured PA signals for the sample collected from donor 1.

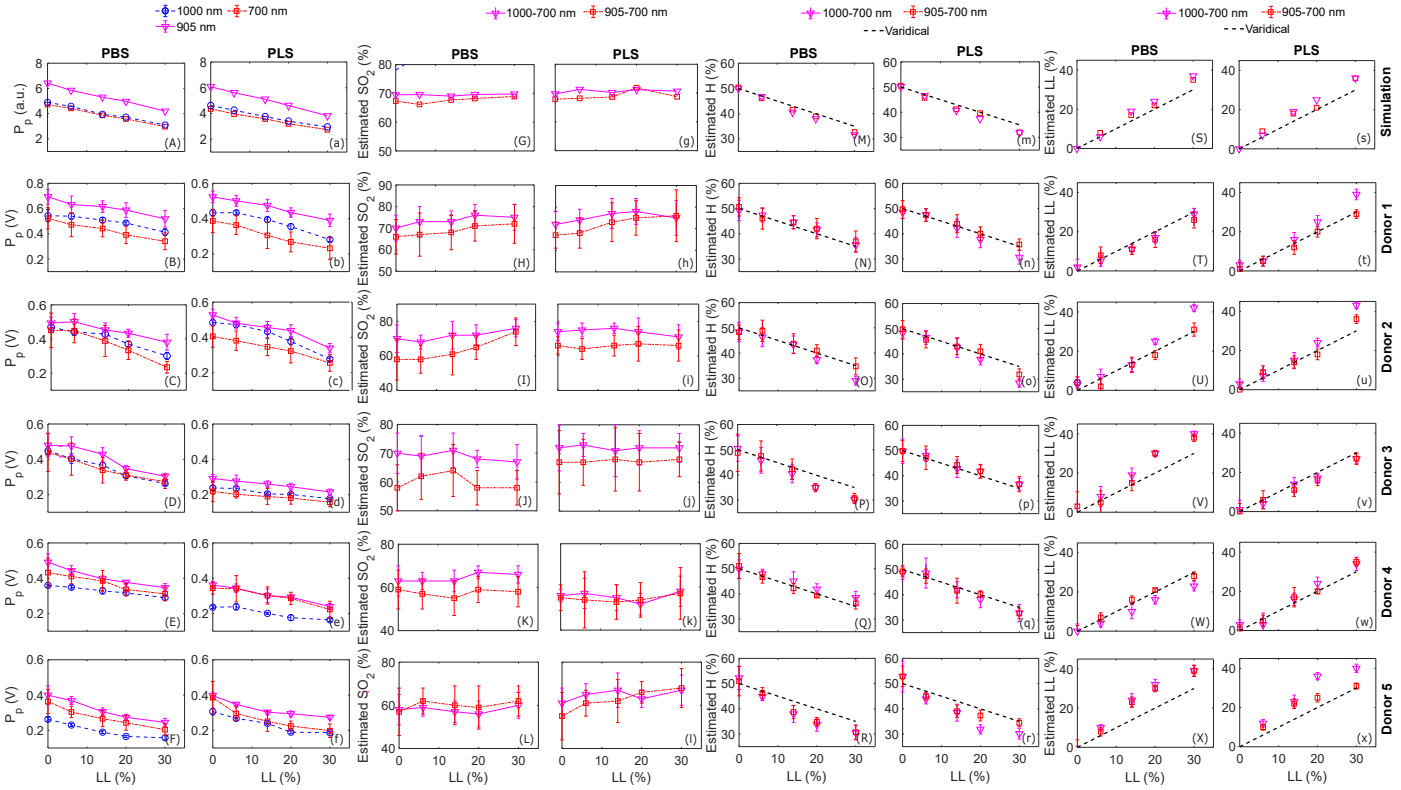

Figure 9. Top row: Analysis of simulated PA signals for the assessment of blood oxygenation, hematocrit and lysis levels. Rows 2-6: Analysis of experimentally measured PA signals for five different donors (see Fig. 3 for details) and quantification of the same parameters (mean±std) using the dual wavelength protocol.

The maximum estimation errors in PBS are approximately 1.6% and 3.6% for these pairs, respectively. In PLS medium, the corresponding errors are 2.6% and 3.9%, respectively. These values are tabulated in Tables 5 and 4 columns 4, 5 and 7, 8; rows 3-7. The SO_2 levels assessed using the 905-1000 nm combination have demonstrated significant fluctuations (data not shown). Logically, this combination is not suitable for the estimations of SO_2, H, and LL, as both wavelengths lie on the same side of the isosbestic point at 800 nm. Accordingly, results for this combination are not shown in Fig. 9.

The estimated H exhibits a linearly decreasing trend as shown in Fig. 9, panels (M) and (m), for PBS and PLS media, respectively, across the same LL range and wavelength combinations. The highest estimation errors in PBS are approximately 8.2%, and 10.9% for the same wavelength pairs as mentioned earlier, respectively. In PLS medium, the respective errors are 10.2%, and 8.4%, respectively. In contrast, Fig. 9, panels (S) and (s) reveal that evaluated LL rises linearly with nominal LL for PBS and PLS media, respectively. The estimation error increases as LL grows. In PBS, the average LL estimation errors are approximately 13.1%, and 19% for the 700-905 nm and 700-1000 nm combinations, respectively. Similarly, in PLS medium, the same errors are 18.1% and 22.3%, respectively. These values are detailed in Tables 5 and 4, columns 2, 3 and 2, 6; rows 3-7.

4.2 Experimental results

Some representative experimentally obtained PA signals at 700, 905 and 1000 nm wavelengths and for LL= 0% and 30% are plotted in Fig. 8 (D)-(F) and (d)-(f). The PA signal amplitude at LL=30% is less compared to that of 0%, as also seen in simulations (left panel of Fig. 8). In general, PA signal strength is higher at 905 nm than the other wavelengths.

Figure 9, panels (B)–(F) and (b)–(f), presents the impact of RBC lysis on peak-to-peak amplitude (P_p, mean $\pm$ std) for two different suspending media, at three different incident optical wavelengths and for blood samples collected from five different individuals (elaborated in Table 3). The lysis level is gradually altered from LL=0 to 30%. The experimental values of P_p show a linear decrease with increasing LL. More specifically, approximately 35, 25 and 24% reduction of PA amplitude can be seen at 700, 905 and 100 nm wavelengths for donor 1 [see Fig. 9(B)].

The SO_2 levels estimated from experimental data do not exhibit any noticeable variation though LL has been changed from LL=0 to 30% as shown in Fig. 9(H). This trend is followed for both wavelength combinations and in both PBS and PLS suspending media [see Fig. 9, panels (H)–(L) and (h)–(l)]. The computed values of blood SO_2 are also inserted in Tables 5 and 4, columns 5 and 8, rows 8-32. In order to validate our findings, the same quantity has also been determined from the optical absorbance spectra measured using a UV-Vis spectrophotometer and the corresponding values are included in columns 4 and 7, Tables 5 and 4. The average SO_2 estimation errors can be found to be around 14.8%, 11.5% for 700-905 nm and 10.2%, 6.0% for 700-1000 nm wavelength pairs in PBS and PLS media, respectively. The first combination clearly shows a little better accuracy than the later wavelength pair. Note that PA method seems to facilitate

physiologically meaningful estimation of the blood SO_2 level since venous blood samples were collected from healthy individuals for which SO_2 level lies roughly between 60–80%.

The assessed H decreases linearly as LL increases [see Fig. 9, panels (N)-(R) and (n)-(r)]. It is clear from these figures that the PA method works very well up to LL$\leq$ 10%. However, its deviation from the veridical line becomes pronounced at higher LL values, particularly at LL= 30%. for the wavelength combinations 700-905 nm and 700-1000 and for both PBS and PLS media across all five donors.

The estimated LL values also vary linearly with nominal LL levels as depicted in Fig. 9, panels (T)-(X) and (t)-(x) and Tables 5 and 4, columns 2, 3, 6 and rows 3-32. As expected, the mismatch between the evaluated and the actual values appears prominent at higher lysis levels, specifically at LL=30%. In general, measured data for donor 5 demonstrate a larger variability compared to the remaining donors.

5 Discussion

One of the primary contributions of this study is the adoption of the biconcave shape of RBCs, as opposed to the commonly assumed spherical geometry. The DDA method was employed to compute the absorption and scattering coefficient factors as well as the anisotropy factor for a single RBC. These parameters were evaluated for various surrounding media (PBS, PLS, PBS/PLS based lyzed media). Subsequently, optical parameters, namely, $\mu_{\text{abs}}^{\text{BS}}$, $\mu_{\text{sca}}^{\text{BS}}$ and g were estimated for different blood samples. These parameters control photon propagation vis-á-vis PA emission from a tissue. DDA provides highly accurate results, but it is computationally intensive and time-consuming. For example, for a single RBC with 125 orientational average, computation time was approximately 3.3 hours at 1000 nm, whereas the time requirement was about 12 hours at 450 nm. Therefore, the computational challenge intensifies at lower wavelengths. It is worthy to point out that the number of dipoles used in this study was about 16×10^5 at 1000 nm and 90×10^5 at 450 nm. The DDA method may not be suitable to numerically quantify the optical parameters of blood samples containing clots or aggregates arising from multicellular interactions. Therefore, alternative methods are needed to efficiently estimate these parameters in such complex biological systems. MC simulations—especially GPU-accelerated versions like MCX—are widely used for estimating bulk optical properties in turbid media [18]. Finite-difference time-domain and finite element method approaches offer full-wave and multiphysics capabilities, making them well-suited for complex or heterogeneous tissues [53], [24]. These alternatives enable scalable and practical optical modeling beyond the scope of DDA.

The numerical values of absorption coefficient, $\mu_{\text{abs}}^{\text{BS}}$, of the blood samples at different lysis levels considered in this study were calculated using Eq. (16) and are tabulated in Table 1, columns 7 and 11, rows 3–17. The absorption values remain constant across all lysis levels at each wavelength. This is because light absorption depends on the total hemoglobin concentration, which does not change with lysis as the initial hematocrit remained fixed at H=50%. The calculated values of $\mu_{\text{abs}}^{\text{BS}}$ provided by the DDSCAT algorithm look very interesting (see Table 2, columns 4 and 9; rows 3-17). It decreases with increasing lysis level. This behavior essentially supports a fact that

Table 4. A comprehensive comparison of numerically and experimentally evaluated SO_2 values and lysis levels (LL) at the dual wavelengths of 700-905 nm.

Blood Sample	PBS				PLS		
	LL (%)	Estimated LL (%)	Estimated SO_2 (%) [UV-Vis]	Estimated SO_2 (%) [PA]	Estimated LL (%)	Estimated SO_2 (%) [UV-Vis]	Estimated SO_2 (%) [PA]
Simulation	0	0.0	68.0	67.9	0.0	68.0	68.3
	6	7 .0	68.0	66.9	8.0	68.0	69.0
	14	16.0	68.0	68.3	16.0	68.0	69.3
	20	23 .0	68.0	67.6	24.0	68.0	69.8
	30	36 .0	68.0	67.5	37.0	68.0	68.3
Donor 1	0	-1.0±3.6	43.0	66.0±8.0	1.0±3.5	43.0	67.0±6.0
	6	8.0±4. 2	0.0	67±10.0	5.0±2.5	0.0	68.0±7.0
	14	11.0±2.6	0.0	68.0±8.0	12.0±3.5	0.0	73.0±9.0
	20	16.0±4.0	0.0	71.0±7.0	20.0±2.7	0.0	75.0±8.0
	30	26.0±4.1	46.0	72.0±9.0	29.0±2.1	46.0	76.0±12.0
Donor 2	0	4.0±2.8	43.0	58.0±12.0	0.0±3.5	43.0	66.0±5.0
	6	2.0±4.2	0.0	58.0±8.0	9.0±3.2	0.0	64.0±6.0
	14	13.0±3.9	0.0	61.0±12.0	14.0±3.2	0.0	66.0±6.0
	20	18.0±2.3	0.0	65.0±7.0	18.0±2.7	0.0	67.0±10.0
	30	31.0±3.3	43.0	74.0±8.0	36.0±2.2	43.0	66.0±9.0
Donor 3	0	3.0±7.3	45.0	58.0±8.0	0.0±4.2	45.0	67. 0±11.0
	6	5.0±5.9	0.0	62.0 ±8.0	6.0±4.6	0.0	67.0±8.0
	14	15.0±4.0	0.0	64.0±9.0	11.0±3.3	0.0	68.0±11.0
	20	30.0±1.4	0.0	58.0±6.0	16.0±2.7	0.0	67.0±10.0
	30	38.0±1.9	44.0	58.0±6.0	27.0±3.0	44.0	68.0±6.0
Donor 4	0	-2.0±4.9	44.0	59.0±9.0	1.0±2.2	44.0	55.0±6.0
	6	7.0±2.3	0.0	57.0±7.0	5.0±2.8	0.0	54.0±13.0
	14	16.0±1.9	0.0	55.0±8.0	17.0±4.9	0.0	53.0±8.0
	20	21.0±0.6	0.0	59.0±6.0	20.0±1.3	0.0	54.0±8.0
	30	28.0±2.2	44.0	58.0±7.0	35.0±2.0	44.0	57.0±12.0
Donor 5	0	-2.0±5.8	45.0	57.0±11.0	-6.0±4.0	45.0	55.0±11.0
	6	8.0±2.2	0.0	62.0±6.0	10.0±1.5	0.0	61.0±6.0
	14	23.0±2.6	0.0	60.0±9.0	22.0±2.4	0.0	62.0±10.0
	20	30.0±1.6	0.0	59.0±10.0	25.0±2.1	0.0	66.0±5.0
	30	39.0±2.8	41.0	62.0±7.0	31.0±1.5	41.0	68.0±9.0

photons might have undergone multiple reflections inside erythrocytes (due to the presence of cell membrane) [42]. Notably, as RBCs experience lysis, the sample became more homogeneous, leading to a reduction in the scattering coefficient ($\mu_{\text{sca}}^{\text{BS}}$) and an expected increase in the anisotropy factor (g). These variations can also be seen from Table 2, columns 6, 7; 11, 12; rows 3-17). The changes of $\mu_{\text{abs}}^{\text{BS}}$, $\mu_{\text{sca}}^{\text{BS}}$ and PA amplitude with RBC lysis (columns 1 and 2 of Fig. 9) are consistent with published results (see Fig. 10 of [42]).

It may be noted that RBCs undergo progressive biochemical and structural changes during storage, such as ATP depletion, increased membrane rigidity, oxidative stress, and ion imbalance. These changes make them more prone to lysis. Factors such as storage temperature, additive solutions, and leukoreduction significantly affect RBC viability.

Table 5. Detailed tabulation of the estimated SO_2 values and lysis levels (LL) determined via numerical and experimental investigations using the wavelength pair of 700-1000 nm.

Blood Sample	PBS				PLS		
	LL (%)	Estimated LL (%)	Estimated SO_2 (%) [UV-Vis]	Estimated SO_2 (%) [PA]	Estimated LL (%)	Estimated SO_2 (%) [UV-Vis]	Estimated SO_2 (%) [PA]
Simulation	0	0.0	68.0	70.5	-1.0	68.0	70.3
	6	7.0	68.0	70.0	8.0	68.0	70.6
	14	18.0	68.0	69.8	18.0	68.0	69.9
	20	25.0	68.0	69.4	26.0	68.0	70.4
	30	38.0	68.0	68.8	36.0	68.0	70.7
Donor 1	0	2.0±4.0	58.0	70.0±6.0	3.0±2.4	58.0	72.0±6.0
	6	5.0±2.6	0.0	73.0±7.0	5.0±2.5	0.0	74.0±5.0
	14	11.0±2.5	0.0	73.0±5.0	16.0±3.6	0.0	77.0±7.0
	20	17.0±2.7	0.0	76.0±5.0	25.0±3.2	0.0	78.0±6.0
	30	29.0±2.8	61.0	75.0±6.0	39.0±2.7	61.0	75.0±8.0
Donor 2	0	3.0±3.8	59.0	70.0 ±8.0	3.0±2.4	59.0	74.0±5.0
	6	7.0±3.8	0.0	68.0±4.0	7.0±2.7	0.0	75.0 ±4.0
	14	13.0±3.4	0.0	72.0 ±8.0	15.0±3.9	0.0	76.0 ±3.0
	20	25.0±1.5	0.0	72.0±6.0	24.0±2. 2	0.0	74.0 ±8.0
	30	42.0±1.7	58.0	76.0±5.0	43.0±1.6	58.0	71.0 ±7.0
Donor 3	0	-1.0±5.0	62.0	70.0±7.0	1.0±4.8	62.0	72.0 ±8.0
	6	8.0±5.0	0.0	69.0 ±7.0	4.0±2.4	0.0	73.0 ±4.0
	14	19.0±3.5	0.0	71.0±6.0	14.0±3.4	0.0	71.0 ±9.0
	20	30.0±1.6	0.0	68.0 ±3.0	17.0±2.5	0.0	72.0±6.0
	30	40.0±1.4	58.0	67.0 ±6.0	27.0±2.3	58.0	72.0±5.0
Donor 4	0	0.0±3.7	62.0	63.0±7.0	3.0±2.4	62.0	56.0±3.0
	6	4.0±1.9	0.0	63.0±4.0	3.0±5.9	0.0	57.0±7.0
	14	10.0±3.6	0.0	63.0±5.0	16.0±3.1	0.0	55.0±6.0
	20	16.0±2.1	0.0	67.0±3.0	24.0±3.2	0.0	52.0±5.0
	30	23.0±2.5	57.0	66.0±4.0	34.0±3.4	57.0	58.0±7.0
Donor 5	0	-4.0±4.5	60.0	58.0±7.0	-6.0±6.1	60.0	61.0 ±7.0
	6	10.0±1.5	0.0	59.0 ±4.0	12.0±1.9	0.0	65.0 ±5.0
	14	24.0±3.3	0.0	57.0±5.0	23.0±3.3	0.0	67.0 ±8.0
	20	32.0±2.6	0.0	56.0±6.0	36.0±1.8	0.0	63.0 ±4.0
	30	39.0±2.7	61.0	60.0±6.0	40.0±2.1	61.0	67.0 ±7.0

Additionally, exposure of phosphatidylserine and hemoglobin release due to lysis can trigger inflammation and transfusion-related complications, emphasizing the need for proper storage and monitoring of blood bags [21, 62]. The methodology reported herein may find an application to examine the health of stored blood. As found, 700-905 nm or 700-1000 nm wavelength pair may be utilized for simultaneous quantification of the oxygenation, hematocrit and lysis levels of such blood samples. Attempts will be made in future to achieve this end.

The technique may be further developed to quantify the lysis levels in vivo which may be useful for monitoring patients. Note that this method can accurately quantify the lysis level when the initial hematocrit is known. In practice, it is unlikely to have the knowledge of H before hand. This challenge may be solved using machine learning

(ML), deep learning (DL) and artificial intelligence (AI) approaches, which may enable accurate and concurrent estimations of H, LL and SO_2 in vivo.

6 Conclusions

The study investigates lysis process of RBCs using both numerical and experimental tools involving PAs. The DDA effectively captured the structural effects of RBCs, despite initial refractive index calculations did not incorporate cellular features. The estimation accuracy for H reached up to 90% for 700-905 nm and 700-1000 nm wavelength pairs up to LL=14%. Interestingly, SO_2 remained relatively stable across the LL range of 0-30%. The nominal and predicted LL levels are found to be strongly correlated with correlation coefficient $\approx$ 90%. Among all tested combinations, the wavelength pairs 700-905 and 700-1000 nm have been found to be optimal for the simultaneous determination of H, LL and SO_2 parameters of blood samples in practice.

Acknowledgement

SP thanks the members of the Biomedical Imaging Laboratory (BMIL), IIIT Allahabad for their continuous cooperation and support. Numerous discussions with laboratory members are also highly acknowledged. The authors are thankful to Mr. Vinod Tiwari, Mr. Anil Tiwari, Blood Bank, Swaroop Rani Nehru Hospital and Mr. Vinod Pathak, Health Center, IIIT Allahabad for providing blood samples. HSP acknowledges the support received from Dr. S. K. Majumder, Head, Laser Biomedical Applications Division, Raja Ramanna Centre for Advanced Technology, Indore (MP), India. The work was supported by the ICMR, DBT and ANRF grants (# 56/2/2020-Hae/BMS, # BT/PR44547/MED/32/791/2021 and # CRG/2023/003278, respectively).

Conflicts of interests:

The authors declare that there are no competing interests.

Data availability:

All data needed to evaluate the conclusions in the paper are present in the paper and/or the Supplementary Materials. Additional data related to this paper may be requested from the authors.

References

1. S. AKBAR, Q. AIN, R. RASHEED, A. ASIF, K. A. AHMAD, and R. RASHED. Prevalence, risk factors, and clinical outcomes of anemia among adult males and females attending a general medicine outpatient department. a cross-sectional study.

2. ANSI. *"American National Standard for Safe Use of Lasers"*. Laser Inst of America.

3. S. Banerjee, S. Sarkar, S. Saha, S. K. Hira, and S. Karmakar. Observing temporal variation in hemolysis through photoacoustics with a low cost laser diode based system. *Scientific Reports*, 13(1):7002, 2023.

4. E. Beutler. Hemolytic anemia due to chemical and physical agents. *The New England Journal of Medicine*, 344(14):1033–1039, 2001.

5. L. Bi and P. Yang. Modeling of light scattering by biconcave and deformed red blood cells with the invariant imbedding t-matrix method. *Journal of Biomedical Optics*, 18(5):055001–055001, 2013.

6. D. Biswas, S. Vasudevan, G. C. Chen, and N. Sharma. Quantitative photoacoustic characterization of blood clot in blood: A mechanobiological assessment through spectral information. *Review of Scientific Instruments*, 88(2), 2017.

7. F. J. Bodera, M. J. McVey, K. Sathiyamoorthy, and M. C. Kolios. Detection of clot formation & lysis in-vitro using high frequency photoacoustic imaging & frequency analysis. *Photoacoustics*, 30:100487, 2023.

8. N. Bosschaart, G. J. Edelman, M. C. Aalders, T. G. van Leeuwen, and D. J. Faber. A literature review and novel theoretical approach on the optical properties of whole blood. *Lasers in Medical Science*, 29:453–479, 2014.

9. J. Brunker and P. Beard. Acoustic resolution photoacoustic doppler velocimetry in blood-mimicking fluids. *Scientific reports*, 6(1):20902, 2016.

10. M. D. Cappellini and G. Fiorelli. Glucose-6-phosphate dehydrogenase deficiency. *Lancet*, 371(9606):64–74, 2008.

11. H. DeVoe. Optical properties of molecular aggregates. i. classical model of electronic absorption and refraction. *The Journal of chemical physics*, 41(2):393–400, 1964.

12. B. T. Draine. The discrete-dipole approximation and its application to interstellar graphite grains. *Astrophysical Journal, Part 1 (ISSN 0004-637X), vol. 333, Oct. 15, 1988, p. 848-872.*, 333:848–872, 1988.

13. B. T. Draine and P. J. Flatau. Discrete-dipole approximation for scattering calculations. *Josa a*, 11(4):1491–1499, 1994.

14. B. T. Draine and P. J. Flatau. Discrete-dipole approximation for periodic targets: theory and tests. *Josa a*, 25(11):2693–2703, 2008.

15. B. T. Draine and J. Goodman. Beyond clausius-mossotti-wave propagation on a polarizable point lattice and the discrete dipole approximation. *Astrophysical Journal, Part 1 (ISSN 0004-637X), vol. 405, no. 2, p. 685-697.*, 405:685–697, 1993.

16. E. Efimenko, Y. A. Malkov, A. Murzanev, and A. Stepanov. Scattering of intense femtosecond laser radiation at water aerosol in backward direction. *Applied Physics B*, 121(4):483–488, 2015.

17. R. O. Esenaliev, I. V. Larina, K. V. Larin, D. J. Deyo, M. Motamedi, and D. S. Prough. Optoacoustic technique for noninvasive monitoring of blood oxygenation: a feasibility study. *Applied Optics*, 41(22):4722–4731, 2002.

18. Q. Fang and D. A. Boas. Monte carlo simulation of photon migration in 3d turbid media accelerated by graphics processing units. *Optics express*, 17(22):20178–20190, 2009.

19. M. Fribel. Determination of optical properties of human blood in the spectral range 250 to 1100 nm using monte carlo simulations with hematocrit-dependent effective scattering phase functions. *Journal of Biomedical Optics*, 11(3):34921, 2006.

20. O. A. Godin. Wentzel–kramers–brillouin approximation for atmospheric waves. *Journal of Fluid Mechanics*, 777:260–290, 2015.

21. J. R. Hess. Red cell changes during storage. *Transfusion and Apheresis Science*, 43(1):51–59, 2010.

22. J. Hudson and J. Heritage. The use of the born approximation in seismic scattering problems. *Geophysical Journal International*, 66(1):221–240, 1981.

23. E. Hysi, R. K. Saha, and M. C. Kolios. Photoacoustic ultrasound spectroscopy for assessing red blood cell aggregation and oxygenation. *Journal of Biomedical Optics*, 17(12):125006, 2012.

24. J.-M. Jin. *The finite element method in electromagnetics*. John Wiley & Sons, 2015.

25. A. B. Karpiouk, S. R. Aglyamov, S. Mallidi, J. Shah, W. G. Scott, J. M. Rubin, and S. Y. Emelianov. Combined ultrasound and photoacoustic imaging to detect and stage deep vein thrombosis: phantom and ex vivo studies. *Journal of Biomedical Optics*, 13(5):054061, 2008.

26. G. J. Kato, M. T. Gladwin, and M. H. Steinberg. Deconstructing sickle cell disease: Reacting to and repairing the vaso-occlusive crisis. *Nature Reviews Disease Primers*, 3(1):123–132, 2007.

27. A. Kaushik and R. K. Saha. Characterization of normal and deformed red blood cells using simulated differential photoacoustic cross-section spectral data. *Journal of Physics Communications*, 5(3):035007, 2021.

28. A. A. Khan and M. A. Rahman. Hemoglobin-induced kidney injury: Mechanisms and treatment. *Journal of Nephrology*, 29(4):213–221, 2016.

29. H. Kirschner. The role of oxidative stress in hemolysis. *Journal of Hematology & Oncology*, 8(1):34–40, 2015.

30. E. Li, Z. Zhang, Z. He, X. Xu, G. Liu, and Q. Li. Smoothed finite element method with exact solutions in heat transfer problems. *International Journal of Heat and Mass Transfer*, 78:1219–1231, 2014.

31. H. Li, L. Lin, and S. Xie. Refractive index of human whole blood with different types in the visible and near-infrared ranges. In *Laser-Tissue Interaction XI: Photochemical, Photothermal, and Photomechanical*, volume 3914, pages 517–521. SPIE, 2000.

32. M. I. Mishchenko, J. W. Hovenier, and L. D. Travis. Light scattering by nonspherical particles: theory, measurements, and applications. *Measurement Science and Technology*, 11(12):1827–1827, 2000.

33. N. Mohandas and P. G. Gallagher. Red cell membrane: Past, present, and future. *Blood*, 112(10):3939–3948, 2008.

34. S. Padmanabhan and J. Prakash. Deep tissue sensing of chiral molecules using polarization-enhanced photoacoustics. *Science Advances*, 11(12):eado8012, 2025.

35. P. P. Pai, P. K. Sanki, and S. Banerjee. A photoacoustics based continuous non-invasive blood glucose monitoring system. In *2015 IEEE International Symposium on Medical Measurements and Applications (MeMeA) Proceedings*, pages 106–111. IEEE, 2015.

36. S. Paul, H. S. Patel, V. Misra, R. Rani, A. K. Sahoo, and R. K. Saha. Numerical and in vitro experimental studies for assessing the blood hematocrit and oxygenation with the dual-wavelength photoacoustics. *Photoacoustics*, 39:100642, 2024.

37. S. Paul, H. S. Patel, and R. K. Saha. Quantitative evaluation of the impact of variation of optical parameters on the estimation of blood hematocrit and oxygen saturation for dual-wavelength photoacoustics. *JOSA A*, 41(6):1128–1139, 2024.

38. I. Y. Petrov, D. S. Prough, Y. Petrov, S. N. Henkel, R. Seeton, and R. O. Esenaliev. Simultaneous measurements of total hemoglobin concentration and blood oxygenation with laser diode-based optoacoustic system. In *Photons Plus Ultrasound: Imaging and Sensing 2017*, volume 10064, pages 111–116. SPIE, 2017.

39. Y. Y. Petrov, I. Y. Petrova, I. A. Patrikeev, R. O. Esenaliev, and D. S. Prough. Multiwavelength optoacoustic system for noninvasive monitoring of cerebral venous oxygenation: a pilot clinical test in the internal jugular vein. *Optics letters*, 31(12):1827–1829, 2006.

40. E. M. Purcell and C. R. Pennypacker. Scattering and absorption of light by nonspherical dielectric grains. *Astrophysical Journal, Vol. 186, pp. 705-714 (1973)*, 186:705–714, 1973.

41. D. C. Rees, T. N. Williams, and M. T. Gladwin. Sickle-cell disease. *The Lancet*, 376(9757):2018–2031, 2010.

42. A. Roggan, M. Friebel, K. Dörschel, A. Hahn, and G. J. Mueller. Optical properties of circulating human blood in the wavelength range 400-2500 nm. *Journal of biomedical optics*, 4(1):36–46, 1999.

43. S. Safiri, A.-A. Kolahi, M. Noori, S. A. Nejadghaderi, N. Karamzad, N. L. Bragazzi, M. J. Sullman, and et al. Burden of anemia and its underlying causes in 204 countries and territories, 1990–2019: results from the global burden of disease study 2019. *Journal of Hematology & Oncology*, 14:1–16, 2021.

44. R. K. Saha. Computational modeling of photoacoustic signals from mixtures of melanoma and red blood cells. *The Journal of the Acoustical Society of America*, 136(4):2039–2049, 2014.

45. R. K. Saha, S. Karmakar, and M. Roy. Photoacoustic response of suspended and hemolyzed red blood cells. *Applied Physics Letters*, 103(4), 2013.

46. R. K. Saha, S. Karmakar, and M. Roy. Probing confined and unconfined hemoglobin molecules with photoacoustics. In *Photons Plus Ultrasound: Imaging and Sensing 2014*, volume 8943, pages 681–686. SPIE, 2014.

47. R. K. Saha and M. C. Kolios. Effects of erythrocyte oxygenation on optoacoustic signals. *Journal of Biomedical Optics*, 16(11):115003, 2011.

48. R. K. Saha and M. C. Kolios. A simulation study on photoacoustic signals from red blood cells. *The Journal of the Acoustical Society of America*, 129(5):2935–2943, 2011.

49. T. Saratoon, T. Tarvainen, B. Cox, and S. Arridge. A gradient-based method for quantitative photoacoustic tomography using the radiative transfer equation. *Inverse Problems*, 29(7):075006, 2013.

50. L. I. Schiff. *Quantum Mechanics*. McGraw Hill Education, 1968.

51. A. Shander, M. D. Cappellini, and L. T. Goodnough. Anemia and blood transfusion: A brief narrative review. *Hematology*, 2009(1):1–6, 2009.

52. K. A. Shapovalov. The geometry and optical models of the erythrocyte. *measurements*, 1:4, 2020.

53. A. Taflove, S. C. Hagness, and M. Piket-May. Computational electromagnetics: the finite-difference time-domain method. *The Electrical Engineering Handbook*, 3(629-670):15, 2005.

54. H.-P. Tan, H.-L. Yi, P.-Y. Wang, L.-M. Ruan, and T. W. Tong. Ray tracing method for transient coupled heat transfer in an anisotropic scattering layer. *International journal of heat and mass transfer*, 47(19-20):4045–4059, 2004.

55. T. Van Buren, G. Arwatz, and A. J. Smits. A simple method to monitor hemolysis in real time. *Scientific reports*, 10(1):5101, 2020.

56. J. J. Wang, A. T. Chen, Y. P. Han, and P. Briard. Light scattering from an optically anisotropic particle illuminated by an arbitrary shaped beam. *Journal of Quantitative Spectroscopy and Radiative Transfer*, 167:135–144, 2015.

57. L. Wang. Monte carlo modeling of photon transport in multi-layered tissues. *Computer methods and programs in biomedicine*, 4:131–146, 1995.

58. N. J. White. Plasmodium falciparum and p. vivax malaria. *The Lancet*, 383(9918):1082–1093, 2018.

59. W. J. Wiscombe. Improved mie scattering algorithms. *Applied optics*, 19(9):1505–1509, 1980.

60. A. C. Yadem, J. N. Armstrong, M. Sarimollaoglu, C. Kiki Massa, J.-M. Ndifo, Y. A. Menyaev, A. Mbe, K. Richards, M. Wade, Y. Zeng, et al. Noninvasive in vivo photoacoustic detection of malaria with cytophone in cameroon. *Nature Communications*, 15(1):9228, 2024.

61. L. Yao, Y. Sun, and H. Jiang. Quantitative photoacoustic tomography based on the radiative transfer equation. *Optics Letters*, 34(12):1765–1767, 2009.

62. T. Yoshida, M. Prudent, and A. D'Alessandro. Red blood cell storage lesion: causes and potential clinical consequences. *Blood Transfusion*, 17(1):27–52, 2019.

63. Y. L. Yung. Variational principle for scattering of light by dielectric particles. *Applied Optics*, 17(23):3707–3709, 1978.

64. A. Zanella and W. Barcellini. Autoimmune hemolytic anemias. *Blood Reviews*, 28(3):91–102, 2014.